

PRODUCTION OF SECONDARIES IN HIGH ENERGY d+Au COLLISIONS

C. Merino, C. Pajares, and Yu. M. Shabelski*

Departamento de Física de Partículas, Facultade de Física,
and Instituto Galego de Altas Enerxías (IGAE),
Universidade de Santiago de Compostela, Galicia, Spain
E-mail: merino@fpaxp1.usc.es, pajares@fpaxp1.usc.es

* Permanent address: Petersburg Nuclear Physics Institute,
Gatchina, St.Petersburg 188350 Russia
E-mail: shabelsk@thd.pnpi.spb.ru

A b s t r a c t

In the framework of Quark-Gluon String Model we calculate the inclusive spectra of secondaries produced in d+Au collisions at intermediate (CERN SPS) and at much higher (RHIC) energies. The results of numerical calculations at intermediate energies are in reasonable agreement with the data. At RHIC energies numerically large inelastic screening corrections (percolation effects) should be accounted for in calculations. We extract these effects from the existing RHIC experimental data on minimum bias and central d+Au collisions. The predictions for p+Au interactions at LHC energy are also given.

PACS. 25.75.Dw Particle and resonance production

1 Introduction

The Quark–Gluon String Model (QGSM) and the Dual Parton Model (DPM) are based on the Dual Topological Unitarization (DTU) and describe quantitatively many features of high energy production processes, including the inclusive spectra of different secondary hadrons, their multiplicities and multiplicity distributions, etc., both in hadron–nucleon and hadron–nucleus collisions at fixed target energies, as well as the main features of secondary production at collider energies. The model parameters were fixed [1-7] by comparison of the calculations with experimental data.

The inclusive densities of different secondaries produced in pp collisions at $\sqrt{s} = 200$ GeV in midrapidity region were reasonably described in [8]. In the present paper we calculate in the QGSM the inclusive spectra of secondaries produced in d+Au collisions both at intermediate (CERN SPS, $\sqrt{s_{NN}} = 19.4$ GeV) and much higher (RHIC, $\sqrt{s_{NN}} = 200$ GeV) energies. We also present some predictions for LHC energies.

In the QGSM high energy interactions are considered as proceeding via the exchange of one or several Pomerons, and all elastic and inelastic processes result from cutting through or between Pomerons [9]. Inclusive spectra of hadrons are related to the corresponding fragmentation functions of quarks and diquarks, which are constructed using the Reggeon counting rules [10].

In the case of interaction with a nuclear target the Multiple Scattering Theory (Gribov-Glauber Theory) is used, what allows to consider the interaction with the nuclear target as the superposition of interactions with different numbers of target nucleons.

The radius of a deuteron is rather large in the strong interaction scale, so we can assume that the proton and the neutron in the deuteron interact independently with heavy nuclei. However, sometimes only one nucleon interacts, the second one being a spectator. The average number $\langle N_d \rangle$ of the deuteron nucleons interacting with a heavy nucleus A in a minimum bias collision is determined by the cross sections of secondary production in NA and dA collisions [11]

$$\langle N_d \rangle = \frac{A\sigma_{NA}^{prod}}{\sigma_{dA}^{prod}} \quad (1)$$

and the inclusive spectrum $dn/dy|_{dA}$ of any secondary particle produced in a d+A collision is equal to the product of N_d times the spectrum in a N+A collision:

$$dn/dy|_{dA} = \langle N_d \rangle \cdot dn/dy|_{NA} . \quad (2)$$

In the case of central collisions $\langle N_d \rangle$ can be calculated with the help of Glauber Theory [12], while the values of $dn/dy|_{NA}$ should be those calculated for central N+A collisions [13].

2 Inclusive spectra of secondary hadrons in the Quark-Gluon String Model

For the quantitative predictions one needs a model for multiparticle production and we have used the QGSM in the numerical calculations presented below.

We consider a nucleon as a system of three gluon strings connected to three valence quarks and joint at the point called “string junction” (SJ) [14-16], as it is shown in Fig. 1. Sea quarks are produced by radiation (possibly, via some non-perturbative mechanism) inside the gluon strings.

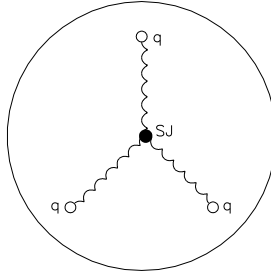


Figure 1: Composite structure of a baryon in string models. Quarks are shown by open points.

As mentioned above, high energy hadron–nucleon and hadron–nucleus interactions are considered in the QGSM as proceeding via the exchange of one or several Pomerons. Each Pomeron corresponds to a cylinder diagram (see Fig. 2a) that, when cutted, produces two showers of secondaries as it is shown in Fig. 2b. The inclusive spectrum of secondaries is determined by the convolution of diquark, valence quark, and sea quark distributions, $u(x, n)$, in the incident particles with the fragmentation functions, $G(z)$, of quarks and diquarks into secondary hadrons. The diquark and quark distribution functions depend on the number n of cut Pomerons in the considered diagram.

In the case of a nucleon target the inclusive spectrum of a secondary hadron h has the form [1]:

$$\frac{x_E}{\sigma_{inel}} \frac{d\sigma}{dx_F} = \frac{1}{\sigma_{inel}} \frac{d\sigma}{dy} = \sum_{n=1}^{\infty} w_n \phi_n^h(x) \quad , \quad (3)$$

where the functions $\phi_n^h(x)$ determine the contribution of diagrams with n cut Pomerons and w_n is the probability of this process [17]. Here we neglect the diffraction dissociation contributions of diffraction which are comparatively small in most of the processes considered below, since they are important mainly for secondary production in the large x_F region that is not significant in the present calculations.

For pp collisions

$$\phi_{pp}^h(x) = f_{qq}^h(x_+, n) \cdot f_q^h(x_-, n) + f_q^h(x_+, n) \cdot f_{qq}^h(x_-, n) + 2(n-1) f_s^h(x_+, n) \cdot f_s^h(x_-, n) \quad , \quad (4)$$

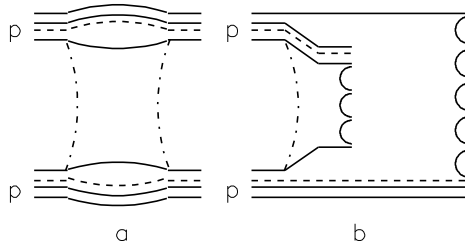


Figure 2: Cylinder diagram (cylinder is shown by dash-dotted curves) corresponding to the one-Pomeron exchange contribution to elastic pp scattering (a), and the corresponding cut diagram which represents its contribution to the inelastic pp cross section (b). Quarks are shown by solid curves and string junctions by dashed lines.

$$x_{\pm} = \frac{1}{2}[\sqrt{4m_T^2/s + x^2} \pm x] , \quad (5)$$

where f_{qq} , f_q , and f_s correspond to the contributions of diquarks, valence quarks, and sea quarks, respectively.

These contributions are determined by the convolution of the diquark and quark distributions with the fragmentation functions, e.g.,

$$f_q^h(x_+, n) = \int_{x_+}^1 u_q(x_1, n) G_q^h(x_+/x_1) dx_1 . \quad (6)$$

The diquark and quark distributions, as well as the fragmentation functions, are determined by Regge intercepts [10].

In the case of nuclear targets we should consider the possibility of one or several Pomeron cuts in each of the ν blobs of hadron-nucleon inelastic interactions, as well as cuts between Pomerons. For example, for a pA collision one of the cut Pomerons links a diquark and a valence quark of the projectile proton with a valence quark and diquark of one target nucleon, while other Pomerons link the sea quark-antiquark pairs of the projectile proton with diquarks and valence quarks of other target nucleons and also with sea quark-antiquark pairs of nucleons in the target.

In particular, and as one example, one of the diagrams contributing to for the inelastic interaction with two target nucleons is shown in Fig. 3. In the blob of the proton-nucleon 1 inelastic interaction one Pomeron is cut, and in the blob of the proton-nucleon 2 interaction two Pomerons are cut. It is essential to take into account all digrams with every possible Pomeron configuration and permutation. The process shown in Fig. 3 satisfies the condition [18-21] that the absorptive parts of the hadron-nucleus amplitude are determined by the combination of the absorptive parts of the hadron-nucleon amplitudes.

Let us consider the case of inelastic interactions with ν target nucleons, n cut Pomerons in hA collisions ($n \geq \nu$), and n_i cut Pomerons connecting with the i -th target nucleon

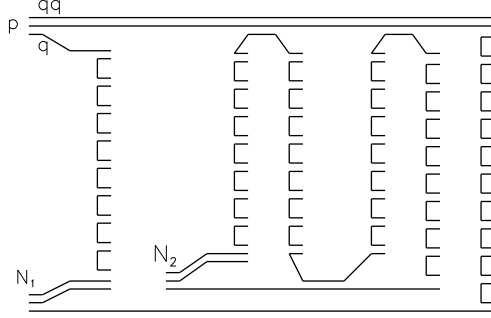


Figure 3: One of the diagrams for the inelastic interaction of an incident proton with two target nucleons N_1 and N_2 in a pA collision.

($1 \leq n_i \leq n - \nu + 1$), i.e. for the diagram in Fig. 3 $\nu = 2$, $n = 3$, $n_1 = 1$, $n_2 = 2$. We define the relative weight of the contribution with n_i cut Pomerons in every hN blob as $w_{n_i}^{hN}$. For the inclusive spectrum of the secondary hadron h produced in a pA collision we obtain [5]

$$\begin{aligned} \frac{dn}{dy} = \frac{x_E}{\sigma_{pA}^{prod}} \frac{d\sigma}{dx_F} &= \sum_{\nu=1}^A V_{pA}^{(\nu)} \left\{ \sum_{n=\nu}^{\infty} \sum_{n_1=1}^{n-\nu+1} \cdots \sum_{n_\nu=1}^{n-\nu+1} \prod_{l=1}^{\nu} w_{n_l}^{pN} \times \right. \\ &\times [f_{qq}^h(x_+, n) f_q^h(x_-, n_l) + f_q^h(x_+, n) f_{qq}^h(x_-, n_l) + \\ &+ \sum_{m=1}^{2n-2} f_s^h(x_+, n) f_{qq,q,s}^h(x_-, n_m)] \left. \right\} , \end{aligned} \quad (7)$$

where $V_{pA}^{(\nu)}$ is the probability of pure inelastic (nondiffractive) interactions with ν target nucleons, and we should account for all possible Pomeron permutations and for the difference in quark content of the protons and neutrons in the target.

In particular, the contribution of the diagram in Fig. 3 to the inclusive spectrum is

$$\begin{aligned} \frac{x_E}{\sigma_{pA}^{prod}} \frac{d\sigma}{dx_F} &= 2V_{pA}^{(2)} w_1^{pN_1} w_2^{pN_2} \left\{ f_{qq}^h(x_+, 3) f_q^h(x_-, 1) + \right. \\ &+ f_q^h(x_+, 3) f_{qq}^h(x_-, 1) + f_s^h(x_+, 3) [f_{qq}^h(x_-, 2) + f_q^h(x_-, 2) + \\ &+ 2f_s^h(x_-, 2)] \left. \right\} . \end{aligned} \quad (8)$$

The diquark and quark distributions and the fragmentation functions here are the same as in the case of a nucleon target.

3 Inclusive spectra in p+Au and d+Au collisions at CERN SPS energy

The QGSM gives a reasonable description [5, 22] of the inclusive spectra of different secondaries produced on nuclear targets at energies $\sqrt{s_{NN}} = 14\text{-}30$ GeV.

In Fig. 4 we compare our results obtained by using Eqs. (2), (7) for the minimum bias p+Au and for 0-43% central d+Au collisions with the experimental data in the rapidity distributions of negatively charged secondaries at $\sqrt{s_{NN}} = 19.4$ GeV [23] in laboratory system. The calculated value of the average number of interacting beam nucleons in these central collisions is $\langle N_d \rangle = 1.93$. For minimum bias interactions we use $\langle N_d \rangle = 1.61$.

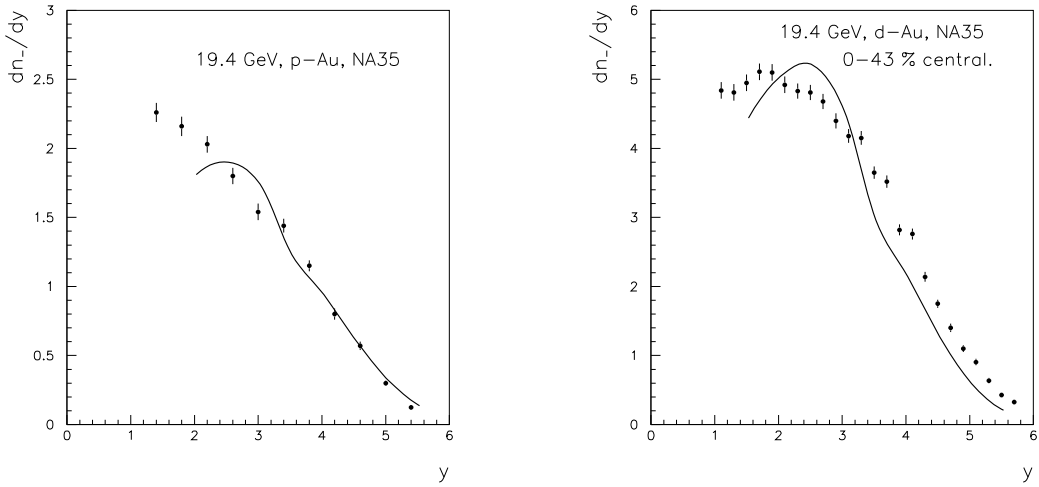


Figure 4: Rapidity distributions of negatively charged secondaries at $\sqrt{s_{NN}} = 19.4$ GeV [23], measured in minimum bias p+Au (left panel) and in 0-43% central d+Au collisions (right panel) together with their description by the QGSM.

In the central region $y_{lab} \sim 3$, as well as in the beam fragmentation region the agreement for both p+Au and d+Au cases is reasonable. The differences between the calculated curves and the data are not larger than 10%. In the target fragmentation region, (at lab. rapidities $y_{lab} \leq 1.5$) our curves underestimate the data, what can be connected with Fermi-motion and/or intranuclear cascade contributions. By comparing these results with those in [1, 5, 6, 22] one can see that the A-dependence of the inclusive spectra is reasonably represented by the QGSM, and that our assumption of independent interaction of the proton and the neutron in deuteron with the target in d+A collisions agrees with the experimental data.

The NA35 Collaboration has also presented the rapidity distributions of net protons and net Λ -hyperons measured in minimum bias p+Au, and similar distributions of net protons in 0-43% central d+Au collisions. Following [24], for the calculation of these

distributions in the QGSM we consider three different sources of the net baryon charge. The first one is the fragmentation of the diquark, that gives rise to a leading baryon carrying the initial SJ (Fig. 5a). A second possibility is to produce a leading meson in the first break-up of the string and a baryon in the subsequent break-up [10, 25] (Fig. 5b). In these two cases the baryon number transfer is only possible for short distances in rapidity. In the third case shown in Fig. 5c, both initial valence quarks recombine with sea antiquarks into mesons M , and a secondary baryon is formed by the SJ together with three sea quarks.

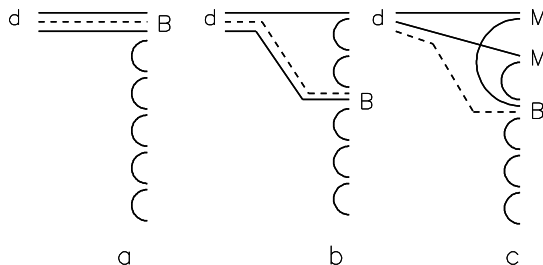


Figure 5: QGSM diagrams describing secondary baryon B production by diquark d : initial SJ together with two valence quarks and one sea quark (a), initial SJ together with one valence quark and two sea quarks (b), and initial SJ together with three sea quarks (c).

The corresponding fragmentation functions for the secondary baryon B production can be written as follows (see [24] for more details):

$$G_{qq}^B(z) = a_N v_{qq} \cdot z^{2.5}, \quad (9)$$

$$G_{qs}^B(z) = a_N v_{qs} \cdot z^2(1-z), \quad (10)$$

$$G_{ss}^B(z) = a_N \varepsilon v_{ss} \cdot z^{1-\alpha_{SJ}}(1-z)^2 \quad (11)$$

for the processes shown in Figs. 5a, 5b, and 5c, respectively, and where a_N is the normalization parameter, and v_{qq} , v_{qs} , v_{ss} are the relative probabilities for different baryons production that can be found by simple quark combinatorics [26, 27]. The fraction z of the incident baryon energy carried by the secondary baryon decreases from Fig. 5a to Fig. 5c, whereas the mean rapidity gap between the incident and secondary baryons increases. The contribution of the graph in Fig. 5c contains a coefficient ε which determines the small probability of such baryon number transfer.

The values of the parameters α_{SJ} and ε which correctly describe [28–33] all the data concerning baryon number transfer at high energies were presented in [28] :

$$\alpha_{SJ} = 0.9 \quad \text{and} \quad \varepsilon = 0.024. \quad (12)$$

In Fig. 6 we compare the results of our calculations of net baryon production in p+Au and central d+Au collisions with experimental data [23]. The normalization and general trends are reproduced quite reasonably. The contribution of SJ diffusion turns out to be more important for secondary Λ - $\bar{\Lambda}$ -hyperon production.

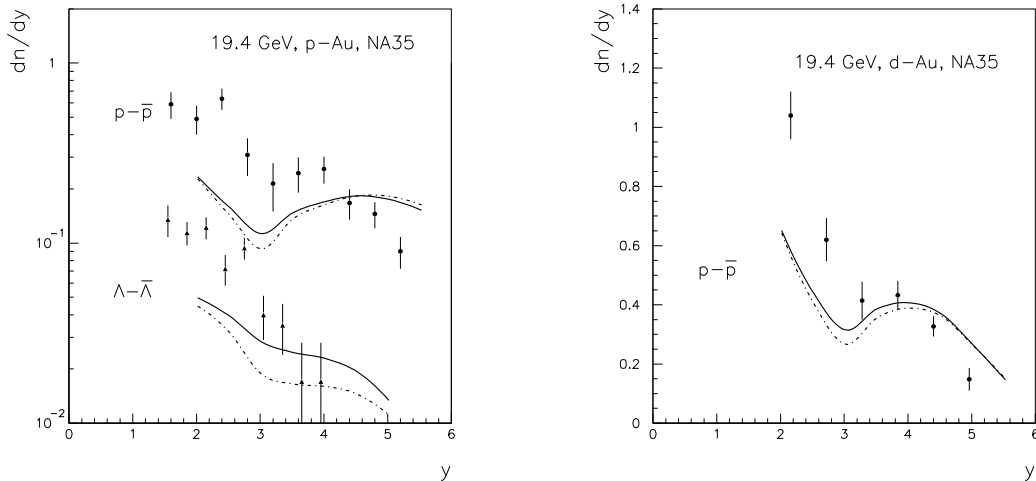


Figure 6: Lab. rapidity distributions of net protons and net Λ -hyperons, measured in minimum bias p+Au (left panel) and similar distributions of net protons in 0-43% central d+Au collisions (right panel) at $\sqrt{s_{NN}} = 19.4$ GeV [23]. The QGSM calculations with and without SJ contributions are shown by solid curves and dashed curves, respectively.

4 Inclusive spectra at RHIC energies

The c.m. pseudorapidity η^* spectra of all charged secondaries in p+p collisions at $\sqrt{s_{NN}} = 200$ GeV were measured by PHOBOS Collaboration [34] and these data are in agreement with the results by the UA5 Collaboration [36]. The PHOBOS data are presented in Fig. 7 together with the QGSM calculation shown by solid curve. In the QGSM calculations we accounted for that [35]

$$\frac{d\sigma}{d\eta^*} = \frac{d\sigma}{dy^*} \cdot \frac{\cosh \eta^*}{\sqrt{m_T^2/p_T^2 + \sinh^2 \eta^*}}, \quad (13)$$

where the pseudorapidity variable η^* can be expressed in terms of the c.m. rapidity variable y^* by

$$\eta^* = \frac{1}{2} \ln \left[\frac{\sqrt{m_T^2 \cosh^2 y^* - m^2} + m_T \sinh y^*}{\sqrt{m_T^2 \cosh^2 y^* - m^2} - m_T \sinh y^*} \right]. \quad (14)$$

The dotted curves in Fig. 7 correspond to the upper limit of 90% confidence level errors. The agreement of QGSM results with experimental points is better than 10%.

The RHIC experimental data for Au+Au collisions [37, 38] give clear evidence of the inclusive density saturation effects which reduce the inclusive density about two times in the central (midrapidity) region in comparison with predictions based on the superposition picture [39, 40, 41]. This reduction can be explained in the framework of the inelastic screening corrections [42]. The effect is very small for integrated cross

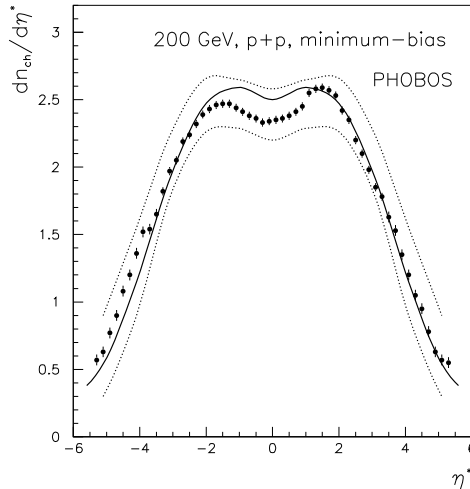


Figure 7: C.m. pseudorapidity distribution of charged secondaries produced in minimum bias p+p collisions at $\sqrt{s} = 200$ GeV [34]. The QGSM calculation is shown by solid curve.

sections (many of them are determined only by geometry), but it is very important [42] for the calculations of secondary multiplicities and inclusive densities at high energies.

Following the estimations in [42], the RHIC energies are just of the order of magnitude needed to observe this effect. The inelastic screening can make [42] the inclusive density in the midrapidity region decrease about two times at RHIC energies and about three times at LHC energies in comparison with the calculation without inelastic screening.

However, all estimations are model dependent. The numerical contribution of multipomeron diagrams is rather unclear due to the very many unknown vertices in the multipomeron diagrams. The number of parameters can be reduced in some models, for example in [42] the Schwimmer model [43] was used for the numerical estimations.

Another (model dependent) possibility to estimate the contribution of the diagrams with Pomeron interaction comes [44, 45, 46, 47] from percolation theory. In this approach one assumes that if two or several Pomerons are overlapping in transverse space, they fuse in only one Pomeron. When all quark-gluon strings (cut Pomerons) are overlapping, the inclusive density saturates, reaching its maximal value at a given impact parameter. This approach has only one free parameter η called percolation parameter

$$\eta = N_s \frac{r_s^2}{R^2} \langle r(y) \rangle, \quad (15)$$

with N_s the number of produced strings, r_s the string transverse radius, and R the radius of the overlapping area. The factor $\langle r(y) \rangle$ accounts for the fact that the parton density near the ends of the strings is smaller than in the central region, where we define $r(0) = 1$.

At large rapidities we have N_s strings with different parton densities, $r_i(y)$, and

$$N_s \langle r(y) \rangle = \sum_{i=1}^{N_s} r_i(y) . \quad (16)$$

As a result, the bare inclusive density $dn/dy|_{bare}$ is reduced and we obtain

$$dn/dy = F(\eta) \cdot dn/dy|_{bare} , \quad (17)$$

with [47]

$$F(\eta) = \sqrt{\frac{1 - e^{-\eta}}{\eta}} . \quad (18)$$

For the d+A interaction, which we consider as the sum of p+A and n+A interactions (see Eq. (2)) we obtain at RHIC energy $\sqrt{s_{NN}} = 200$ GeV for minimum bias interactions $\langle N_d \rangle = 1.61$, which is practically the same value as at CERN SPS energy. This value leads to a number of participant nucleons, $\langle N_{part} \rangle = 8.2$, that is in agreement with the estimation 8.1 ± 0.7 [48]. The value of R^2 in Eq. (15) is the squared average radius of interactions (nucleon radius at not very high energies). The phenomenological estimation of r_s^2 gives $r_s \sim 0.2-0.3$ fm [49] that is in agreement with the estimation of the radius of constituent (dressed) quark [50].

The pseudorapidity spectra of all charged secondaries $dn_{ch}/d\eta^*$ in d+Au collisions at $\sqrt{s_{NN}} = 200$ GeV were measured by PHOBOS [48] and BRAHMS [51] Collaborations. These data allow us to obtain the experimental values of $F(\eta^*)$ as (see Eq. (17))

$$F_{exp}(\eta^*) = \frac{dn/d\eta^*|_{exp}}{dn/d\eta^*|_{bare}} . \quad (19)$$

The corresponding results are presented in Fig. 8 for minimum bias [48] (left panel) and for 0-30% central [51] (right panel) d+Au collisions. Solid lines show the average values of $F_{exp}(\eta^*)$ in the interval $-2 < \eta^* < 1$, where the values of $F_{exp}(\eta^*)$ have minimal values and are compatible with constant behaviour.

The average value of $F_{exp}(\eta^*)$ in the midrapidity region extracted from minimum bias events is $F_{exp}(\eta^*) = 0.615 \pm 0.085$, which corresponds to the pseudorapidity value $\eta^* = 2.4_{-0.75}^{+1.05}$. These error bars are mainly determined by the uncertainty in the calculation of $dn/d\eta^*|_{bare}$. Now we can estimate the values of $\langle r(y) \rangle$ (we assume that $\langle r(y) \rangle = \langle r(\eta^*) \rangle$ in Eq. (15)) as

$$\langle r(y) \rangle = \frac{dn(y)/dy|_{bare}}{dn(y=0)/dy|_{bare}} , \quad (20)$$

and we can calculate the values of $F(\eta^*)$ as a function of pseudorapidity η^* using its normalization at $\eta^* \sim 0$. The results are shown in Fig. 8 by a dashed curve and they are in agreement with the experimental data.

From the analysis of 0-30% central d+Au collisions [51] (right panel in Fig. 8) we obtain the average value of $F_{exp}(\eta^*) = 0.658 \pm 0.092$, which corresponds to the η^* value,

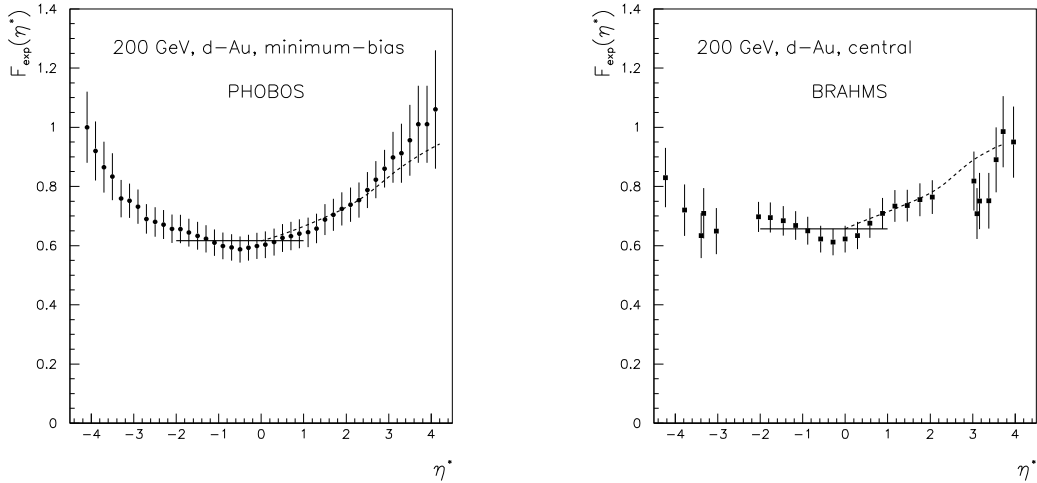


Figure 8: C.m. pseudorapidity distributions of the ratios of $F_{exp}(\eta^*)$ for charged secondaries at $\sqrt{s_{NN}} = 200$ GeV in minimum bias [48] (left panel) and in 0-30% central [51] (right panel) d+Au collisions. Solid lines show the average values of $F_{exp}(\eta^*)$ in the interval $-2 < \eta < 1$. The dashed curves are the values of $F_{exp}(\eta^*)$ using its normalization at $\eta^* = 0$.

$\eta^* = 2_{-0.7}^{+0.95}$. In the same way as in the minimum bias case the estimation of $\langle r(y) \rangle$ allows us now to calculate the pseudorapidity dependence of $F(\eta^*)$ shown in the right panel of Fig. 8 by a dashed curve.

Finally, from the results shown in Fig. 8 we obtain that the value of the percolation parameter η for d+Au collisions in the midrapidity region is rather large, $\eta \geq 1.5$. This implies a significant contribution from the processes with high density parton matter effects. These results are in qualitative agreement with [52].

Let us now consider the absolute values of pseudorapidity distributions for produced charged secondaries $dn_{ch}/d\eta^*$. They are presented in Fig. 9 for the minimum bias [48] (left panel) and 0-30% central [51] (right panel) d+Au collisions at $\sqrt{s_{NN}} = 200$ GeV. The standard QGSM calculations without any percolation contributions (those in denominator of Eq. (19)) are shown by solid curves and they are in evident disagreement with the experimental data.

To account for the percolation effects it is technically more simple to consider the maximal number of pomerons, n_{max} , which can be emitted by one nucleon of the deuteron. In this case all model calculations become rather simple because above the critical value every additional pomeron cannot contribute to the inclusive spectrum. In this scenario we obtain a reasonable agreement with the experimental data (see dashed curves in Fig. 9 for $n_{max} = 13$). This value of n_{max} is slightly larger than the average value of produced strings $\langle N_s \rangle$ (see Eq. (15)). The last value can be estimated as the double (every cut Pomeron corresponds to two strings) product of the average value of cut Pomerons in one non-diffractive NN interaction $\langle n_{NN} \rangle \sim 2.1$ times the average number of interacting

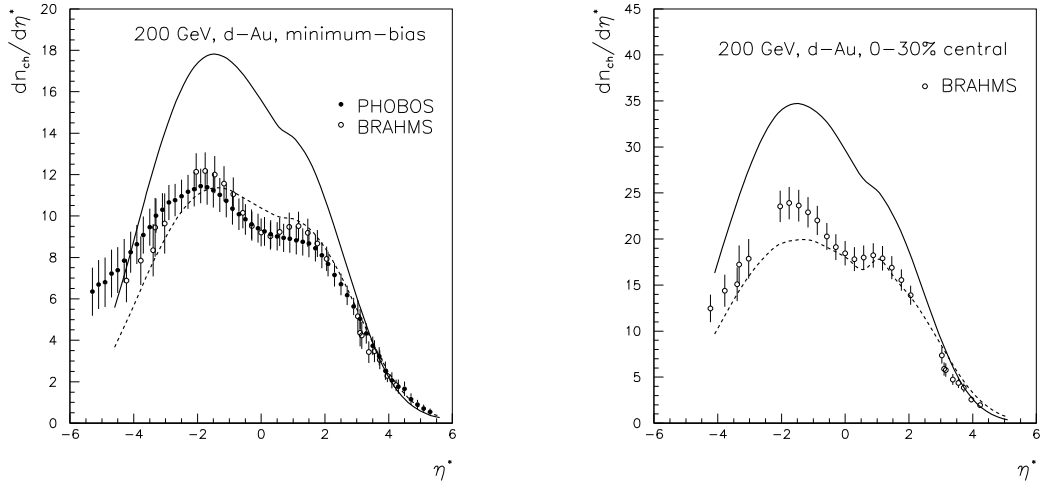


Figure 9: C.m. pseudorapidity distributions of charged secondaries at $\sqrt{s_{NN}} = 200$ GeV measured in minimum bias [48, 51] (left panel) and in 0-30% central [51] (right panel) d+Au collisions, together with their description by the bare QGSM (solid curves), and by taking into account percolation contributions (dashed curves).

nucleons in the Au nucleus $\langle\nu_{NA}\rangle = A\sigma_{NN}^{inel}/\sigma_{NA}^{prod} \sim 5$ at RHIC energy

$$\langle N_s \rangle = 2\langle n_{NN} \rangle \cdot \langle\nu_{NA}\rangle \quad (21)$$

(we have used $\sigma_{NN}^{inel} = 43.4$ mb.) So the percolation effects do not affect the average configurations of Pomerons, but restrict the tails of the distributions.

The yields of Λ and $\bar{\Lambda}$ were measured by STAR Collaboration [53] at RHIC energies in both the minimum bias and 0-20% central d+Au collisions at $\sqrt{s_{NN}} = 200$ GeV. In Fig. 10 we compare the results of our calculations of Λ and $\bar{\Lambda}$ production in minimum bias d+Au collisions with experimental data [53]. The multiplicities of Λ and $\bar{\Lambda}$ are reproduced in a quite reasonable way. The similar calculations of Λ and $\bar{\Lambda}$ production at RHIC energy were also presented in [33].

The same calculations for Λ and $\bar{\Lambda}$ production in 0-20% central d+Au collisions at $\sqrt{s_{NN}} = 200$ GeV [53] are presented in Fig. 11 where the agreement with the data is also good.

5 Predictions for LHC energies

Let us consider the predictions for p+Au (p+Pb) collisions at LHC energy $\sqrt{s} = 8.8$ TeV per nucleon.

The calculated result for the charged particle inclusive density in the midrapidity region, $dn_{ch}/dy(y = 0)$, as a function of initial energy without percolation effects is shown in Fig. 12 (left panel) by solid curve.

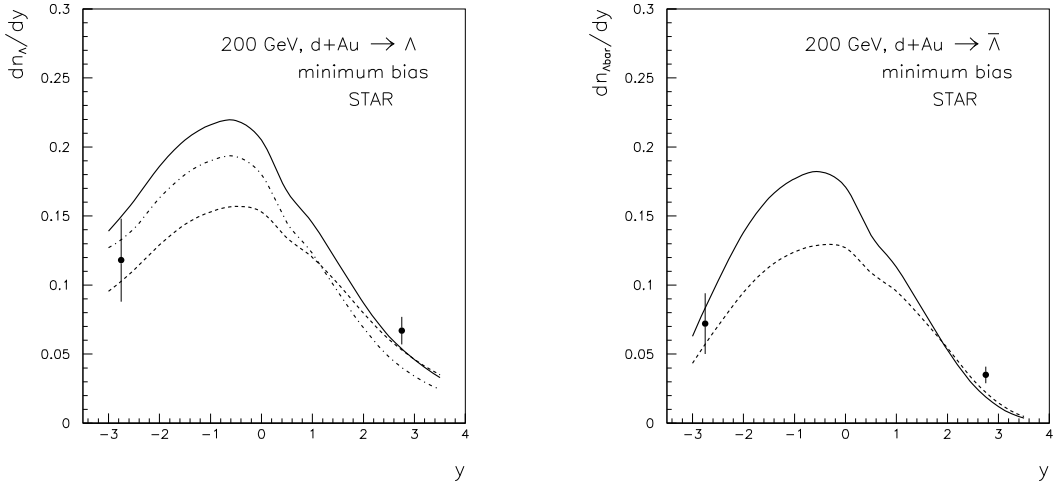


Figure 10: Rapidity distributions of Λ (left panel) and $\bar{\Lambda}$ hyperons (right panel), measured in minimum bias d+Au collisions at $\sqrt{s_{NN}} = 200$ GeV [53]. The QGSM calculations with and without SJ contributions are shown by solid curves and dash-dotted curves, respectively. Dashed curves show the results accounting for percolation effects.

In accounting for the percolation effects we meet the problem of the possible energy dependence of the maximal number of pomerons, n_{max} , which can be emitted by the incident proton.

The result obtained in the simplest variant, in which we neglect any energy dependence of n_{max} , i.e. we use $n_{max} = 13$ at all energies, is shown in the left panel of Fig. 12 by the dashed curve.

At fixed target energies $\sqrt{s_{NN}} = 15-40$ GeV percolation effects are too small to be observed by comparison of the model calculations with experimental data. An additional suppression of the percolation effects at fixed target energies comes from the fact that the strings from the nucleus need some distance from the nucleus position (lab. frame) in rapidity space to fuse (percolation) [54] in the midrapidity (c.m. frame) region, but at relatively low energies this distance is small and percolation effects are mainly absent.

At RHIC energies the percolation effects in $dn_{ch}/dy(y=0)$ are about 1.5-1.7 times larger than at fixed target energies and they can increase until 3 times larger at LHC energy. A so large effect in the LHC case is connected with the fact that at $\sqrt{s_{NN}} = 8.8$ TeV we have $\langle n_{NN} \rangle \sim 3$ and $\langle \nu_{NA} \rangle \sim 8$, so the average value of Pomerons (~ 24) in the minimum bias p+A collision is significantly larger than $n_{max} = 13$.

The percolation effect for $dn_{ch}/dy(y=0)$ at LHC energy would be smaller if we assume that the squared interaction radius R^2 in Eq. (15) increases proportionally to the total inelastic pp cross section, whereas the string transverse radius r_s is constant. In this case, and assuming $\sigma_{NN}^{inel}(\sqrt{s_{NN}} = 8.8 \text{ TeV}) = 75.5 \text{ mb}$, the value of n_{max} can approximately increase proportionally to the $\sigma_{NN}^{inel}(\sqrt{s_{NN}} = 8.8 \text{ TeV})/\sigma_{NN}^{inel}(\sqrt{s_{NN}} = 200$

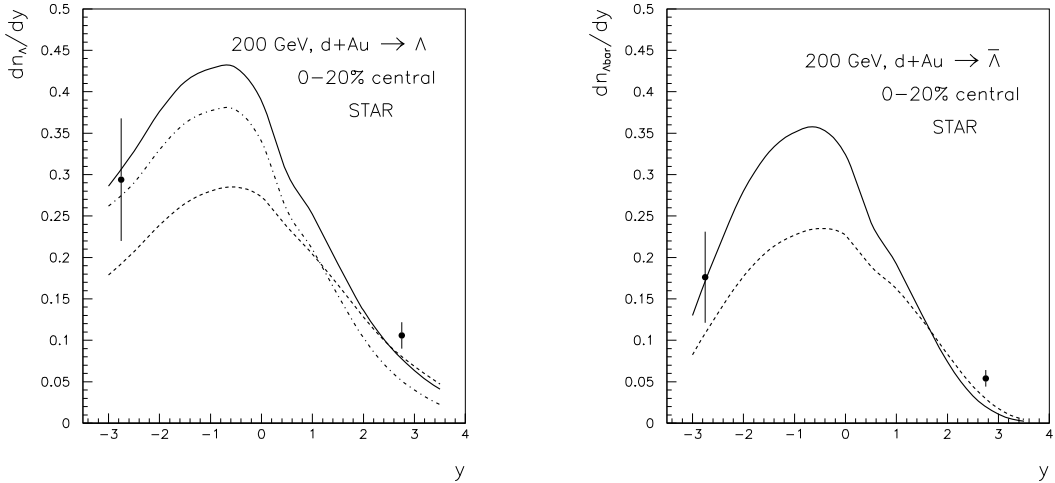


Figure 11: Rapidity distributions of Λ (left panel) and $\bar{\Lambda}$ hyperons (right panel) measured in 0-20% central d+Au collisions at $\sqrt{s_{NN}} = 200$ GeV [53]. All curve specifications are the same as in Fig. 10.

GeV) ratio and we would predict the behaviour shown by the dash-dotted curve in left panel of Fig. 12.

The predicted rapidity distributions of charged secondaries without (solid curve) and with percolation effects with $n_{max} = 13$ (dashed curve) are presented in the right panel of Fig. 12. Our solid curve is rather close to the estimation of [55] but the shape in the maximum is different.

The processes of baryon number transfer via string junction diffusion [24, 28-33] should also be accounted at these so high energies.

6 Conclusions

We show that the QGSM together with the Multiple Scattering Theory can describe on reasonable level the inclusive spectra of secondaries produced in d+Au collisions at CERN SPS energies.

The data of RHIC and their comparison with CERN SPS data show numerically large effects coming from the inelastic screening effects, or Pomeron (secondary particle) density saturation. These effects can be quantitatively described in the percolation approach. It is necessary to say that the scheme used here (the restriction of the number of Pomerons which can be cut in one N+A interaction) is different from the approaches used in Refs. [44, 45, 47], but our scheme seems closer to the point of view of the Parton Model [54, 56]. The numerical difference with [54, 56] comes from the fact that the ratio of r_s^2/R^2 in Eq. (15) is rather small, so the percolation parameter, η , is also small and most of Pomerons can exist without percolating. That is why the effects of Pomeron

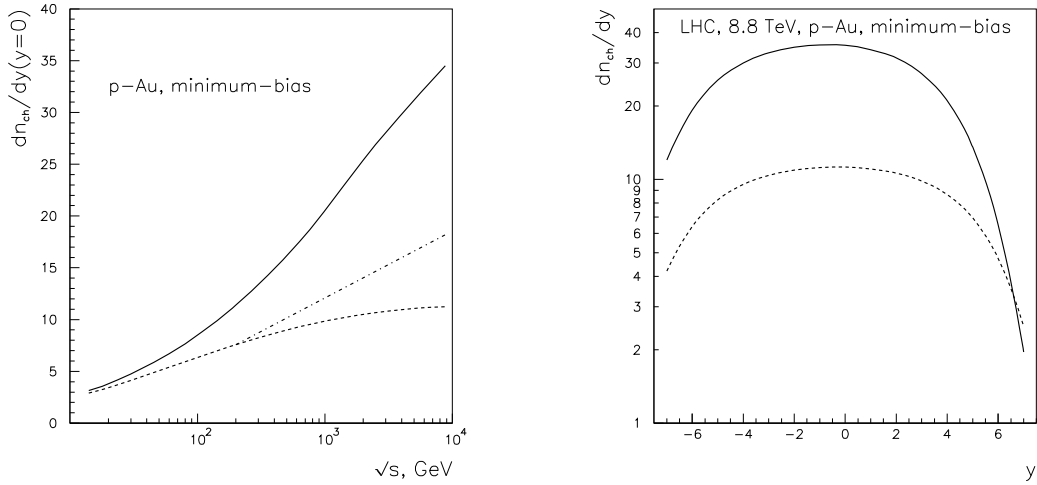


Figure 12: The calculated energy dependence of $dn_{ch}/dy(y=0)$ (left panel) and the predicted rapidity distributions of charged secondaries in p+Au (p+Pb) collisions at LHC energy $\sqrt{s_{NN}} = 8.8$ TeV. The results without and with percolation effects are shown by solid and dashed curves, respectively. Dash-dotted curve in the left panel shows the result with percolation and with accounting for an increase of R^2 with energy proportional to σ_{NN}^{inel} and r_s^2 constant (see Eq. (15)).

(secondary particle) density saturation are small at fixed target energies and they become visible only starting from RHIC energies (see left panel of Fig. 12). These effects can increase with energy if the ratio of r_s^2/R^2 is constant, or they can be practically energy independent if the ratio of $r_s^2/R^2 \sim 1/\sigma_{NN}^{inel}$.

Acknowledgements

We are grateful to N. Armesto and J. Dias de Deus for useful discussions. This paper was supported by Ministerio Educación y Ciencia of Spain under project FPA 2005–01963 and by Xunta de Galicia and, in part, by grants RFBR-07-02-00023 and RSGSS-1124.2003.2.

References

- [1] A. B. Kaidalov, K. A. Ter-Martirosyan, *Yad. Fiz.* **39**, 1545 (1984); **40**, 211 (1984).
- [2] A. B. Kaidalov, O. I. Piskunova, *Yad. Fiz.* **41**, 1278 (1985).
- [3] A. Capella, U. Sukhatme, C. I. Tan, J. Tran Thanh Van, *Phys. Rep.* **236**, 225 (1994).
- [4] A. Capella, J. Tran Thanh Van, *Z. Phys.* **C10**, 249 (1981);
A. Capella, C. Pajares, A. V. Ramallo, *Nucl. Phys.* **B241**, 75 (1984).
- [5] A. B. Kaidalov, K. A. Ter-Martirosyan, Yu. M. Shabelski, *Yad. Fiz.* **43**, 1282 (1986).
- [6] Yu. M. Shabelski, *Yad. Fiz.* **44**, 186 (1986).
- [7] C. Pajares, Yu. M. Shabelski, *Relativistic Nuclear Interactions*, Editorial URSS, Moscow, 2007.
- [8] G. H. Arakelyan, C. Merino, C. Pajares, Yu. M. Shabelski, hep-ph/0709.3174 and accepted for the publication in *Eur. Phys. J. C*.
- [9] V. A. Abramovsky, V. N. Gribov, O. V. Kancheli, *Yad. Fiz.* **18**, 595 (1973).
- [10] A. B. Kaidalov, *Sov. J. Nucl. Phys.* **45**, 902 (1987); *Yad. Fiz.* **43**, 1282 (1986).
- [11] A. Bialas, M. Bleszynski, W. Czyz, *Nucl. Phys.* **B111**, 461 (1976).
- [12] A. P. Cheplakov, A. P. Gasparian, Yu. M. Shabelski, *Sov. J. Nucl. Phys.* **34**, 739 (1981);
C. Pajares, A. V. Ramallo, *Phys. Rev.* **D31**, 2800 (1985).
- [13] Yu. M. Shabelski, *Sov. J. Nucl. Phys.* **50**, 149 (1989).
- [14] X. Artru, *Nucl. Phys.* **B85**, 442 (1975).
- [15] M. Imachi, S. Otsuki, F. Toyoda, *Prog. Theor. Phys.* **52**, 346 (1974); **54**, 280 (1976);
55, 551 (1976).
- [16] G. C. Rossi, G. Veneziano. *Nucl. Phys.* **B123**, 507 (1977).
- [17] K. A. Ter-Martirosyan, *Phys. Lett.* **44B**, 377 (1973).
- [18] Yu. M. Shabelski, *Yad. Fiz.* **26**, 1084 (1977); *Nucl. Phys.* **B132**, 491 (1978).
- [19] L. Bertocchi, D. Treleani, *J. Phys.* **G3**, 147 (1977).
- [20] J. Weis, *Acta Phys. Polonica* **B7**, 85 (1977).

- [21] T. Jaroszewicz et al., Z. Phys. **C1**, 181 (1979).
- [22] Yu. M. Shabelski, Sov.J.Nucl.Phys. **45**, 143 (1987); Z. Phys. **C38**, 569 (1988).
- [23] NA35 Collaboration (T. Alber et al.), Eur. Phys. J. **C2**, 643 (1998).
- [24] G. H. Arakelyan, A. Capella, A. B. Kaidalov, Yu. M. Shabelski, Eur. Phys. J. **C26**, 81 (2002); hep-ph/0103337.
- [25] A. Capella, B. Z. Kopeliovich, Phys. Lett. **B381** 325 (1996).
- [26] V. V. Anisovich, V. M. Shekhter, Nucl. Phys. **B55**, 455 (1973).
- [27] A. Capella, C.-A. Salgado, Phys. Rev. **C60**, 054906 (1999).
- [28] F. Bopp, Yu. M. Shabelski, Yad. Fiz. **68**, 2155 (2005); hep-ph/0406158.
- [29] G. H. Arakelyan, C. Merino, Yu. M. Shabelski, Yad. Fiz. **69**, 911 (2006); hep-ph/0505100;
Phys. Atom. Nucl. **70**, 1110 (2007); hep-ph/0604103;
Eur. Phys. J. **A31**, 519 (2007); hep-ph/0610264;
hep-ph/0707.1491 and accepted for its publication in Eur. Phys. J. C.
- [30] O. I. Piskounova, Phys. Atom. Nucl. **70**, 1110 (2007); hep-ph/0604157.
- [31] F. Bopp, Yu. M. Shabelski, Eur. Phys. J. A **28**, 237 (2006); hep-ph/0603193.
- [32] Yu. M. Shabelski, hep-ph/0705.0947.
- [33] F. W. Bopp et al., Phys. Rev. **C77**, 014904 (2008); hep-ph/0505035.
- [34] PHOBOS Collaboration (B. B. Back et al.), J. Phys. **G30**, S1133 (2004); nucl-ex/0403033.
- [35] D. Kharzeev, E. Levin. Phys. Lett. **B523**, 79 (2001).
- [36] UA5 Collaboration (G. J. Alner et al.), Z. Phys. **C33**, 1 (1986).
- [37] PHOBOS Collaboration (B. B. Back et al.), Phys. Rev. Lett. **85**, 3100 (2000).
- [38] PHENIX Collaboration (K. Adcox et al.), Phys. Rev. Lett. **86**, 500 (2001).
- [39] A. Capella, C. Merino, J. Tran Thanh Van, Phys. Lett. **B265** (1991) 415.
- [40] Yu. M. Shabelski, Z. Phys. **C57**, 409 (1993).
- [41] N. Armesto, C. Pajares, Int. J. Mod. Phys. **A15**, 2019 (2000).
- [42] A. Capella, A. Kaidalov, J. Tran Thanh Van, Heavy Ion Phys. **9**, 169 (1999).

- [43] A. Schwimmer, Nucl. Phys. **B94**, 445 (1975).
- [44] J. Dias de Deus, R. Ugoccioni, A. Rodrigues, Phys. Lett. **B458**, 402 (1999); Eur. Phys. J. **C16**, 537 (2000).
- [45] M. A. Braun, C. Pajares, Phys. Rev. Lett. **85**, 4864 (2000).
- [46] J. Dias de Deus, Yu. M. Shabelski, Eur. Phys. J. **A20**, 457 (2004);
P. Brogueira, J. Dias de Deus, C. Pajares, Phys. Rev. **C75**, 054908 (2007).
- [47] M. A. Braun, C. Pajares, Eur. Phys. J. **C16**, 2019 (2000).
- [48] PHOBOS Collaboration (B. B. Back et al.), Phys. Rev. Lett. **93**, 082301 (2004);
nucl-ex/0311009.
- [49] N. Armesto, M. A. Braun, E. G. Ferreira, C. Pajares, Phys. Rev. Lett. **77**, 3736 (1996).
- [50] V. V. Anisovich, M. N. Kobrinsky, J. Nyiri, Yu. M. Shabelski, Soviet Physics – Uspekhi **144**, 553 (1984); *Quark Model and High Energy Collisions*, World Scientific, Singapore, 1985.
- [51] BRAHMS Collaboration (I. Arsene et al.), Phys. Rev. Lett. **94**, 032301 (2005);
nucl-ex/0401025.
- [52] D. Kharzeev, E. Levin, M. Nardi, Nucl. Phys. **A730**, 448 (2004); Nucl. Phys. **A743**, 329 (2004).
- [53] STAR Collaboration (B. I. Abelev et al.), nucl-ex/0607.0472
- [54] O. V. Kancheli, JETP Lett. **18**, 274 (1973).
- [55] J. Dias de Deus, J. G. Milhano, Nucl. Phys. **A795**, 98 (2007).
- [56] G. V. Davidenko, N. N. Nikolaev, Yad. Fiz. **24**, 772 (1976).